

Lagrangian Ellipsoid Diagnostics for Stochastic Hydrodynamics: Source–Sink Modeling of Deforming Particle Clouds^a

Michael (Misha) Chertkov^{1,2,†}

¹*Graduate Interdisciplinary Program in Applied Mathematics,
University of Arizona, Tucson, Arizona 85721, USA*

²*Department of Mathematics, University of Arizona, Tucson, Arizona 85721, USA*

(Dated: May 28, 2026)

arXiv:2605.27606v1 [physics.flu-dyn] 26 May 2026

^a This paper is dedicated to the memory of Misha Stepanov, who was tragically killed after being struck by a car on May 7, 2026. Over the last eight years, Misha and the author had many discussions on Lagrangian closures and related reduced descriptions of turbulent transport. In his unpublished notes [1], Misha was the first to observe the saturation of Lagrangian anisotropy in a setting similar to the one studied here. This observation became one of the central empirical and methodological motivations for the present work.

Abstract

We propose the *Löwner–John deform-cloud scheme* as a minimal Lagrangian diagnostic of an incompressible stochastic flow with an inertial range: we release a volume-filled cloud of particles at the ultraviolet scale and track the co-evolution of $g(t)$, the inertia tensor of the minimum-volume enclosing ellipsoid (MEE) of the cloud, and $M(t)$, the velocity gradient coarse-grained over the ellipsoid. We validate the scheme on a two-dimensional isotropic, incompressible, Gaussian–Hölder random velocity at exponent $\zeta = 1/3$, constructed in spectral form with Ornstein–Uhlenbeck dynamics of the Fourier amplitudes. For this synthetic flow we show that the empirical train has an $O(1)$, broadly fluctuating log-aspect-ratio σ of the ellipsoid; a scaling behavior of the average $\|M\|^2$; and an approximate tensor-level strain–vorticity balance $\chi(r) = \frac{\text{Var}(\omega|r)}{\text{Var}(s_+|r) + \text{Var}(s_\times|r)} \simeq 1$, where $r = (\det g)^{1/4}$ is the ellipsoid scale, ω is the antisymmetric component of the coarse-grained gradient, and s_+, s_\times are the two components of its strain (symmetric part of M).

We then formulate reduced modeling of the (M, g) train as physics-informed generator identification within a parameterized stochastic ODE framework. In intrinsic variables $(v, \sigma, A, \omega, \alpha)$, with $v = \log r$, $A = |S|$ the strain amplitude, and α the doubled angle between the principal strain direction and the ellipsoid axis, the aspect-ratio dynamics separates into the source–sink form $\dot{\sigma} = 2A \cos \alpha + R_\sigma$. The resulting reduced model treats A and ω as scale-dependent stochastic drivers, represents the alignment angle by a stationary von–Mises bias, and closes the Löwner–John projection residual by the affine form $R_\sigma = a_0(r) + a_1(r)\sigma$. The model is intentionally interpretable rather than black-box: it identifies the aligned-strain source and the geometric ellipsoid-relaxation sink responsible for the observed $O(1)$ cloud aspect ratio.

The significance of the construction is methodological: it provides a portable Lagrangian route from particle-cloud data to physically readable finite-dimensional stochastic dynamics, offering a controlled baseline for future applications to convective and obstacle-generated turbulent flows.

I. INTRODUCTION AND ROADMAP

This paper presents three modeling constructions and the relations between them: a Lagrangian diagnostic, a synthetic 2D random-flow class, and a physics-informed reduced

[†] chertkov@arizona.edu

model. The diagnostic and the synthetic flow together produce an empirical matrix-valued train.

The reduced-model part then shows how this train can be converted into physically interpretable source–sink terms and a small stochastic closure¹ The purpose is methodological: to demonstrate, in a controlled setting, a pipeline that can later be adapted to DNS and experimental particle data in more realistic turbulence flows.

a. Section II: the Löwner–John deform-cloud scheme. The bridge between a flow simulation and a reduced description of multi-particle Lagrangian dynamics is an algorithm that maps a deforming particle cloud to a low-dimensional structured time series. We seed N tracers uniformly in a ball of radius r_0 , chosen of the order of the ultraviolet cutoff scale of the flow, and advect them by the velocity field. At each time we fit the minimum-volume enclosing ellipsoid of the cloud and record its symmetric and positive-definite inertia tensor $g(t)$. For the synthetic flow considered here, the velocity field is known spectrally, so we also compute the spatial average of the velocity gradient over the same ellipsoid. The primary empirical object is therefore the state-space train

$$x(t) = (g(t), M(t)) \in \text{SPD}(2) \times \mathfrak{sl}(2), \quad \dim x(t) = 3 + 3 = 6. \quad (1)$$

where traceless $M(t)$ is the ellipsoid-averaged coarse-grained gradient. All empirical claims in Part III refer to this train unless stated otherwise.

b. Why the outer ellipsoid. The minimum-volume enclosing ellipsoid (MEE) is the most direct ellipsoidal summary of the cloud’s outer envelope. It records the scale and anisotropy to which an initially ultraviolet cloud has been stretched as it expands into the inertial range. This makes it the natural first baseline for the deform-cloud diagnostic. The maximum-volume inscribed ellipsoid is also geometrically meaningful, but it responds to thinning and folding rather than to the outer extent of the cloud.²

The full diagnostic-to-modeling workflow is summarized in Fig. 1: the volume-filled cloud is advected, replaced by its MEE, mapped to the train (M, g) , and then reduced to the intrinsic variables used in the source–sink analysis.

¹ In this sense the paper connects the older Lagrangian tetrad program [2] and the recent physics-informed Lagrangian modeling line [3–6] on the MachinE Learning of Turbulence (MELT) collaboration Los Alamos National Laboratory and University of Arizona collaboration, but with the finite-cloud geometry retained explicitly.

² Equivalently, the MEE asks how far the cloud has spread, while the inner ellipsoid asks how much coherent interior volume remains. Both are useful, but they should be calibrated and interpreted separately.

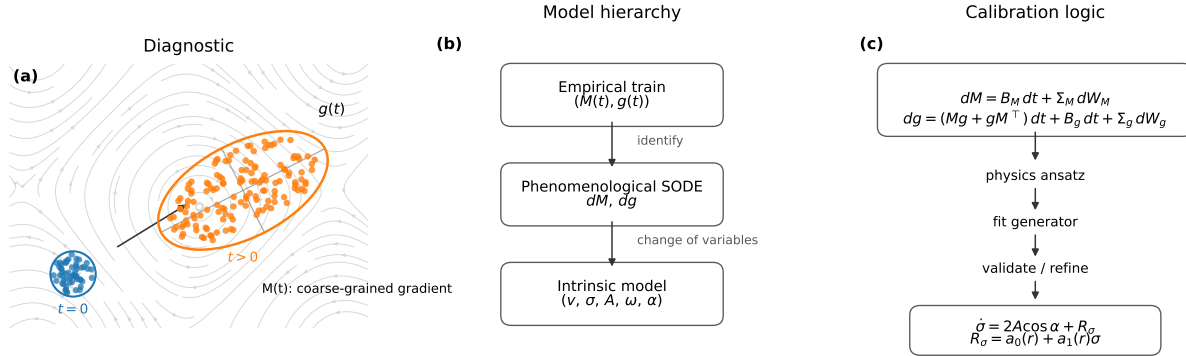


Figure 1. Schematic summary of the Lagrangian ellipsoid diagnostic and the reduced-modeling pipeline. (a) A volume-filled tracer cloud is initialized at the ultraviolet scale, advected by the synthetic incompressible flow, and summarized at later times by its minimum-volume enclosing ellipsoid $g(t)$. The velocity gradient is coarse-grained over the same ellipsoidal region, giving the empirical train variable $M(t)$. (b) Model hierarchy used in the paper: the empirical train $(M(t), g(t))$ motivates a phenomenological stochastic ordinary differential equation for dM and dg , which is then reduced to intrinsic variables $(v, \sigma, A, \omega, \alpha)$. (c) Physics-informed calibration loop. Starting from the general stochastic ordinary differential equation (SODE), we choose a physically motivated parametrization, estimate short-time generator terms from the empirical train, validate by forward simulation, and refine the closure. The final aspect-ratio dynamics is organized around the source–sink form $\dot{\sigma} = 2A \cos \alpha + R_\sigma$, with the Löwner–John residual represented by $R_\sigma = a_0(r) + a_1(r)\sigma$.

c. Section III: Kraichnan-style synthetic flow. The baseline flow is an isotropic Fourier-spectral incompressible random field with prescribed Hölder roughness and finite-time, scale-dependent Ornstein–Uhlenbeck memory of the Fourier amplitudes. We use a sine-sector restriction, so the origin is a fixed point of the velocity field; this gives a constructive sweeping-free, quasi-Lagrangian frame centered at the cloud. The flow is deliberately simpler than Navier–Stokes turbulence: it has prescribed Gaussian spatial statistics, controlled roughness, and no cascade dynamics or coherent structures. Its role is not to replace turbulence, but to provide a clean baseline on which the deform-cloud diagnostic and the reduced-model identification can be understood before being transferred to DNS or experiments.

d. Section IV: Empirical Phenomenology. The empirical measurements are model-free but physically structured. We ask whether the ellipsoid shape reaches an $O(1)$ statistical

regime, whether the conditional distributions of the log-aspect-ratio σ collapse or retain visible scale dependence, and how the coarse-grained gradient variance $\langle |M|^2 | r \rangle$ scales with ellipsoid size. We also examine non-Gaussianity of the rescaled gradient components, the corrected tensor-level strain–vorticity balance

$$\chi(r) = \frac{\text{Var}(\omega | r)}{\text{Var}(s_+ | r) + \text{Var}(s_\times | r)},$$

and the joint alignment statistics between the ellipsoid axis and the principal strain direction. These observations define the empirical targets that any reduced model must reproduce by forward simulation, not by direct curve fitting of final observables.

e. Section V: physics-informed generator identification. The reduced-model part starts from the same phenomenological principle as the Lagrangian tetrad model of [2], here projected to two dimensions and adapted to the Löwner–John ellipsoid train. If an ellipsoid were a material object advected by a locally linear incompressible velocity field, i.e. by a Batchelor flow [7], its inertia tensor would satisfy

$$\dot{g} = Mg + gM^\top. \quad (2)$$

The MEE, however, is not a material ellipsoid: it is a convex-geometric summary of a deforming particle cloud. Likewise, the coarse-grained gradient M is not a closed deterministic variable. We therefore write the general phenomenological stochastic dynamics as

$$dM = B_M(M, g; r) dt + \Sigma_M(M, g; r) dW_M, \quad (3)$$

$$dg = (Mg + gM^\top) dt + B_g(M, g; r) dt + \Sigma_g(M, g; r) dW_g. \quad (4)$$

Here dW_M and dW_g are Wiener differentials. The first term in the g equation is the known material-ellipsoid kinematics (2), whereas $B_M, \Sigma_M, B_g, \Sigma_g$ parameterize the unresolved coarse-grained gradient dynamics, finite-cloud fluctuations, and the Löwner–John projection residual. The task is not to fit arbitrary black boxes for these functions. It is to tighten their parametrization by iterating between physical considerations, short-time generator estimates, forward validation on the empirical train, and failure diagnosis.

In practice this loop leads us from the laboratory-frame variables (M, g) to the following

intrinsic variables:

$$v \doteq \log r, \quad r \doteq (\det g)^{1/4}, \quad \text{the logarithmic ellipsoid scale,} \quad (5a)$$

$$\sigma \doteq \frac{1}{2} \log \frac{\lambda_+(g)}{\lambda_-(g)}, \quad \text{the log-aspect-ratio of the ellipsoid,} \quad (5b)$$

$$A \doteq |S|, \quad S \doteq \frac{1}{2}(M + M^\top), \quad \text{the strain amplitude,} \quad (5c)$$

$$\omega \doteq \frac{1}{2}(M_{21} - M_{12}), \quad \text{the scalar vorticity,} \quad (5d)$$

$$\alpha = 2(\theta_S - \theta_g), \quad \text{the doubled alignment angle.} \quad (5e)$$

Here $\lambda_+(g) \geq \lambda_-(g) > 0$ are the eigenvalues of g , θ_g is the orientation of the major axis of the ellipsoid, and θ_S is the principal stretching direction of the symmetric strain tensor S .

In the variables (5), the aspect-ratio dynamics exposes the source–sink balance

$$\dot{\sigma} = 2A \cos \alpha + R_\sigma. \quad (6)$$

The source $2A \cos \alpha$ is the stretching contribution of the strain in the ellipsoid frame. The residual R_σ is the effective Löwner–John projection correction: it represents the difference between the observed MEE evolution and the material-ellipsoid kinematics (2). We will see that the final low-dimensional closure keeps the physical source $2A \cos \alpha$, models A and ω as scale-dependent stochastic drivers, represents the alignment angle through a stationary von–Mises bias, and closes the Löwner–John residual by the affine form

$$R_\sigma = a_0(r) + a_1(r)\sigma. \quad (7)$$

The resulting model is intentionally modest: it is a controlled example of physics-informed generator identification, not a universal turbulence closure. Its main explanatory role is to turn the observed statistical saturation of ellipsoid anisotropy into an open-box source–sink mechanism: aligned strain creates anisotropy, while the Löwner–John residual provides the effective geometric relaxation that limits it.

II. THE LÖWNER–JOHN DEFORM-CLOUD SCHEME: STATE, SCHEME, AND THE (M, g) TRAIN

A. The Lagrangian state space

a. The deformed blob. Consider a Lagrangian fluid blob in a two-dimensional incompressible flow, initialized as a disc of radius r_0 . Incompressibility preserves the blob’s area exactly; the velocity field stretches and folds the blob so that its perimeter grows without bound while its enclosed area stays at πr_0^2 . The blob’s shape is, at any finite time, a complicated and generally non-convex region of the plane. The deform-cloud scheme replaces this convoluted shape by a single ellipsoidal summary at each instant.

b. Two Löwner–John ellipsoids. For any compact set $K \subset \mathbb{R}^d$, or more precisely for its convex hull $\text{conv}(K)$, there are two canonical ellipsoidal summaries, classical objects of convex geometry [8]:

1. the *minimum-volume enclosing ellipsoid* (MEE), also called the outer Löwner–John ellipsoid: the smallest ellipsoid containing K ;
2. the *maximum-volume inscribed ellipsoid* (MIE), also called the inner Löwner–John ellipsoid: the largest ellipsoid contained in $\text{conv}(K)$.

Both ellipsoids are unique when $\text{conv}(K)$ is full-dimensional. They satisfy the geometric sandwich

$$\text{MIE}(K) \subseteq \text{conv}(K) \subseteq \text{MEE}(K),$$

where the left inclusion refers to the inscribed ellipsoid of the convex hull. The two summaries emphasize different aspects of the same Lagrangian cloud. The MEE follows the outer envelope and is therefore the natural diagnostic when one wants to measure how far the cloud has spread and how anisotropic its extent has become. The MIE probes the largest coherent ellipsoidal core inside the convex hull and is therefore sensitive to thinning, folding, and loss of interior volume.

In an incompressible two-dimensional flow the material cloud preserves its area, but its convex hull and its outer envelope need not do so. Consequently the MEE and MIE can respond differently to the same deformation. In the present baseline the MEE grows as the

volume-filled ultraviolet cloud expands into the inertial range; the MIE may also grow in this setting, but it encodes a different geometric question. We therefore focus here on the outer Löwner–John, or MEE, train as the primary diagnostic and leave the inner ellipsoid train as the natural complementary construction.

c. Deformation matrix and inertia tensor. Pick two independent edge vectors $r_1, r_2 \in \mathbb{R}^2$ aligned with the fitted ellipsoid’s principal axes (or, equivalently, any two independent edges among three Lagrangian particles representing the cloud). Stack them as the rows of a 2×2 deformation matrix

$$\rho = \begin{pmatrix} r_1^\top \\ r_2^\top \end{pmatrix} \in \mathbb{R}^{2 \times 2}, \quad g \doteq \rho^\top \rho \in \text{SPD}(2). \quad (8)$$

The tensor g is the geometric state of the fitted ellipsoid. Its material reference dynamics is the two-dimensional projection of the Lagrangian tetrad kinematics discussed in the Introduction. If the ellipsoid were advected by a locally linear incompressible velocity field r_a and g would follow Eqs. (2–3). In the present scheme, however, g is not the inertia tensor of a material ellipsoid. It is the inertia tensor of the MEE recomputed from the particle cloud at every time. The discrepancy between the observed \dot{g} and the kinematic term in Eq. (6) is therefore not an error; it is the Löwner–John projection residual that the reduced model must parameterize.

d. State and scale. The Lagrangian ellipsoid state is given by Eq. (1). The ellipsoid’s instantaneous scale is the geometric mean of its principal radii, defined in Eq. (5). Scale-dependent reference parameters in the basic model below are evaluated at $r = r(g)$. The state is intrinsic in the sense that (g, M) transforms naturally under rotations of the laboratory frame and the dynamics is rotation-equivariant.

e. Principal-axes parametrisation. The inertia tensor admits the unique decomposition

$$g = R(\theta) \text{diag}(e^{2v+\sigma}, e^{2v-\sigma}) R(\theta)^\top, \quad (9)$$

with $\sigma \geq 0$ the log-aspect-ratio, v the log-volume coordinate ($\det g = e^{4v}$, $r = e^v$), $\theta \in [0, \pi)$ the principal-axes orientation, and $R(\theta)$ the orthogonal rotation by angle θ . This is the natural parametrisation in which the basic ellipsoid SDE simplifies to scalar equations on (v, σ, θ) .

f. Historical motivation. The state (g, M) coincides with the 2D restriction of the Lagrangian tetrad model introduced in [2] as a phenomenology for three-dimensional turbulence. The motivation for that work was inherited from the Lagrangian-zero-mode analysis of anomalous scaling in the passive-scalar Kraichnan model [9–11]: just as multi-point Lagrangian dynamics provided the right technical language for passive-scalar anomalous scaling, the tetrad — a multi-particle Lagrangian object whose joint geometry resolves the velocity gradient as a coarse-grained matrix — was proposed as the minimal Lagrangian object resolving the gradient of Navier–Stokes flow. The present 2D construction is the analogous reduction with three particles inscribing an ellipsoid; the deform-cloud scheme that follows is the constructive algorithm that maps any flow into this reduced state.

The present paper also continues a more recent program developed in the UA–Los Alamos collaboration on MachinE Learning for Turbulence (MELT), where Lagrangian particle-based representations were used to construct physics-informed reduced models of turbulent transport. That program led to Lagrangian large-eddy simulation models based on smooth particle hydrodynamic (SPH)-like particle dynamics and hierarchical reduced Lagrangian closures [4, 5]. The closest predecessor of the present work is the velocity-gradient modeling line, where physics-informed stochastic models were trained on Lagrangian velocity-gradient dynamics in homogeneous isotropic turbulence (HIT) [3, 6]. Those models focused on the local or coarse-grained velocity-gradient tensor along a Lagrangian trajectory, including non-Markovian memory effects, but did not include an explicit finite-cloud geometry variable. The present deform-cloud construction can be viewed as a path forward towards the future complementary step – keep a Markovian state by augmenting the perceived gradient with the ellipsoid geometry g .

B. The scheme: from particle cloud to (M, g)

a. The particle cloud: volumetric ball seeding at the ultra-violet scale. At $t = 0$ seed N Lagrangian tracers uniformly within a ball of radius r_0 centred at the origin of the sweeping-free flow of §III A,

$$\{x_0^{(i)}\}_{i=1}^N \sim \text{Uniform}(B(0, r_0)), \quad (10)$$

with r_0 chosen of the order of the smallest resolved scale of the flow, $r_0 \sim 2\pi/K_{\max}$. The particles are advected as passive tracers,

$$\dot{x}_t^{(i)} = v(x_t^{(i)}, t), \quad i = 1, \dots, N. \quad (11)$$

Volumetric seeding is essential for the present baseline: it gives a genuine cloud interior, avoids the boundary-only artefacts of earlier tests, and makes the enclosing ellipsoid a summary of a volume-filled Lagrangian object rather than of a polygonal ring.

b. The outer Löwner–John ellipsoid. The empirical analysis uses the minimum-volume enclosing ellipsoid (MEE) of the particle cloud. It is the unique ellipsoid

$$\mathcal{E}(t) = \{x \in \mathbb{R}^2 : (x - c(t))^\top g(t)^{-1} (x - c(t)) \leq 1\} \quad (12)$$

with minimum area containing all tracers. Computationally we obtain it by Khachiyan’s algorithm [8]. The MEE is used because it follows the outer envelope of the cloud and therefore gives a monotone-in-statistics scale variable as the cloud evolves from the ultraviolet cutoff into the inertial range. The largest inscribed ellipsoid is a natural complementary object, sensitive to thinning and folding of the cloud, but it is not used in the empirical section below. We leave the inner-ellipsoid train for future work so that the first baseline is not complicated by mixing two geometrically different summaries.

c. The coarse-grained velocity gradient. On the synthetic spectral flow we define the perceived gradient as the spatial average of the instantaneous velocity gradient over the MEE,

$$M_{ij}(t) \doteq \frac{1}{|\mathcal{E}(t)|} \int_{\mathcal{E}(t)} \partial_i v_j(x, t) dx. \quad (13)$$

For the sine-sector spectral construction this average has the closed form

$$M_{ij}(t) = \sum_k -2b_k(t) \cos(k \cdot c(t)) \frac{2J_1(\rho_k)}{\rho_k} k_i (\hat{e}_k^\perp)_j, \quad \rho_k = \sqrt{k^\top g(t) k}. \quad (14)$$

The Bessel factor is the ellipsoid average of the Fourier mode over the cloud. It equals one at small argument and decays with oscillations for large argument, thereby implementing a soft, anisotropic low-pass filter at the cloud scale. When the ellipsoid is elongated, modes aligned with the long axis and modes crossing the short axis are filtered differently. This effect should be measured through corrected tensor-level diagnostics such as χ below, not through the trivial component-level factor of two between vorticity and individual strain components.

d. The (M, g) train. The output of the empirical scheme is the time series (1). In two dimensions this is six real numbers per time step: three for the traceless matrix M and three for the symmetric positive matrix g .

e. Computational cost. The MEE computation is dominated by Khachiyan iterations over the cloud points, while the closed-form gradient average costs one pass over the retained Fourier modes. For the synthetic flow this is comparable to a velocity evaluation. For DNS or experimental data, where the spectral formula is unavailable, the same definition would require numerical quadrature of ∇v over the ellipsoid; that operational extension is separate from the present baseline.

C. Why a deeper Lagrangian diagnostic

a. Beyond scalar pair statistics. Standard scalar Lagrangian diagnostics — the mean square pair separation $\langle r^2(t) \rangle$, the finite-size Lyapunov exponent $\lambda(r)$ [12], the n -th-order velocity-increment structure function $S_n(r)$ [9–11] — each compress the trajectory ensemble into one scalar per scale. They are sensitive to the second moment of the coarse-grained velocity gradient distribution at the relevant scale, integrated over orientations; they are insensitive to joint correlations between the gradient and the shape of the deformed blob, to alignment statistics, and to persistence patterns in the orientation of the deformation.

This emphasis on multi-particle geometry is consistent with earlier work on Lagrangian clusters and tetrads, where the shape of three- and four-particle configurations was used to probe stretching and inertial-range dispersion [13, 14]. The distinction here is operational: instead of tracking a fixed few-particle simplex only, we volume-fill a cloud, summarize its outer envelope by the Löwner–John ellipsoid, and couple that geometry to the ellipsoid-averaged gradient M .

The (M, g) train preserves these joint structures. Concretely:

- The alignment between the elongation direction of g , measured by the angle θ , and the principal strain direction of M , measured by θ_S , is encoded by the doubled relative angle $\alpha = 2(\theta_S - \theta)$. This alignment is not, by itself, the saturation mechanism. Rather, it produces the positive source term in the aspect-ratio Eq. (6). The empirical and reduced-model results in §IV and §V show that statistical saturation of σ is a source–sink balance:

the aligned-strain source $2A \cos \alpha$ is compensated, on average, by the negative Löwner–John residual R_σ .

- The persistence of M across its Ornstein–Uhlenbeck correlation time $\tau(r)$, conditional on the current shape $\sigma(t)$, is a Lagrangian observable that scalar pair statistics cannot resolve.
- The conditional distribution $P(\sigma | r)$ at fixed scale, beyond its mean, distinguishes flows that share the same dimensional scaling but differ in their fluctuation structure.

Two flow classes can share identical Finite Size Lyapunov Exponent (FSLE) slopes and pair-dispersion exponents and yet differ markedly in the joint (M, g) statistics — through differences in intermittency, in alignment statistics, in higher-order Lagrangian correlations. Our focus on the deform-cloud scheme of a Kraichnan–Stepanov flow at fixed ζ is intended in the same spirit. The flow is simpler than Navier–Stokes: Gaussian, prescribed Hölder roughness, OU per-mode correlation, no cascade dynamics, no intermittency, and no coherent vortices. Its purpose is not to predict quantitative constants for real turbulence, but to isolate a mechanism and a diagnostic pipeline in a controlled setting. The mechanisms identified here—source–sink balance of ellipsoid anisotropy and scale-dependent perceived-gradient extraction—should be treated as hypotheses to test in richer flows, not as conclusions already established for them.

b. Connection to Lyapunov / Oseledets theory. The log-aspect-ratio $\sigma(t)$ is a finite- r , finite-time analogue of the Lyapunov-exponent spread: as $t \rightarrow \infty$ in a smooth flow, $\sigma(t)/t \rightarrow \lambda_1 - \lambda_2$, the Lyapunov gap [15, 16]. In a rough flow at finite r , $\sigma(t)$ does not grow indefinitely; the empirical statistical saturation we document in §IV is the finite-time, finite- r counterpart of Oseledets’ multiplicative ergodic theorem, captured here intrinsically per Lagrangian cloud without taking an infinite-time limit.

c. Status. The scheme is an *algorithmic Lagrangian diagnostic*: a constructive map from any flow trajectory to the structured (M, g) train. It carries no flow-specific assumptions beyond the choice of ellipsoid summary (MEE here, MIE in subsequent work); it can be applied identically to synthetic Kraichnan–Stepanov data, to DNS-derived Lagrangian data, or to experimental three-particle reconstructions of (g, M) in the laboratory. The portability of the scheme is its principal methodological feature.

III. THE KRAICHNAN–STEPANOV SYNTHETIC FLOW: SPECTRAL CONSTRUCTION OF AN ISOTROPIC INCOMPRESSIBLE RANDOM FLOW

a. Why a synthetic flow. The deform-cloud scheme of Part I is universal but requires a flow on which to be validated. We need a generator of synthetic Lagrangian data with prescribed and controllable statistics. The class we use is the natural isotropic Fourier-spectral random flow with prescribed Hölder roughness, projected to the divergence-free subspace, and made sweeping-free constructively by spectral restriction. We call it the *Kraichnan–Stepanov flow* to honor the two historical contributions on which it builds: the classical delta-correlated-in-time Gaussian random velocity field introduced by R. Kraichnan in his 1968 *Physics of Fluids* paper [17], and the constructive shear-composition realization of an essentially equivalent flow class developed by M. Stepanov in unpublished notes on synthetic-flow inscribed-ellipsoid simulations [1].

b. Construction. On a periodic box $[0, L]^d$ define the velocity field

$$v(x, t) = \sum_{k \in \Lambda} \hat{v}_k(t) e^{i 2\pi k \cdot x / L}, \quad \Lambda = \mathbb{Z}^d \setminus \{0\}, \quad (15)$$

with complex Fourier coefficients $\hat{v}_k \in \mathbb{C}^d$ constrained by reality $\hat{v}_{-k} = \hat{v}_k^*$. Incompressibility, $\nabla \cdot v = 0$, is enforced spectrally as $k \cdot \hat{v}_k = 0$, which we impose by spectral projection:

$$\hat{v}_k(t) = P(k) a_k(t), \quad P(k) \doteq I - \frac{k k^\top}{|k|^2}, \quad (16)$$

with $a_k(t) \in \mathbb{C}^d$ unconstrained complex Gaussian Fourier amplitudes carrying the prescribed statistics. The projection $P(k)$ preserves the rotational symmetry of the underlying distribution of a_k , so if a_k is drawn with rotationally invariant statistics then \hat{v}_k is as well; the flow is then *isotropic by construction*, with no need for any post-hoc averaging over shear directions.

c. Spatial roughness. Take the amplitudes to be Gaussian and mutually independent across wavenumbers, with

$$\mathbb{E}[a_k a_k^*] = E(|k|) I_d, \quad (17)$$

and choose the amplitude spectrum $E(|k|)$ so that the velocity two-point structure function scales as $\mathbb{E}[(v(x) - v(0))^2] \sim |x|^{2\zeta}$ in the inertial range. The correct modal-spectrum exponent in dimension d (see Remark 1) is

$$E(|k|) \propto |k|^{-(2\zeta+d)} \quad (\zeta \in (0, 1], k \in \text{inertial range}). \quad (18)$$

The case $\zeta = 1$ recovers the smooth (Batchelor) regime; $\zeta < 1$ gives a non-differentiable (rough Kraichnan) velocity field. We focus on $\zeta = 1/3$ in this paper, the K41 inertial scaling, which is also the scaling of the inverse energy cascade in two-dimensional Navier–Stokes turbulence [18].

Remark 1 (The 2D modal-spectrum exponent). *The modal-spectrum exponent in dimension d is $2\zeta + d$, not the 1D value $2\zeta + 1$. The relation between the modal spectrum and the shell-integrated spectrum carries a Jacobian factor $|k|^{d-1}$: $E_{\text{shell}}(|k|) \propto |k|^{d-1} \mathbb{E}[|a_k|^2]$, so requiring $E_{\text{shell}}(|k|) \propto |k|^{-(2\zeta+1)}$ (the canonical relation yielding $S_2(r) \propto r^{2\zeta}$) forces $\mathbb{E}[|a_k|^2] \propto |k|^{-(2\zeta+d)}$. Using the 1D exponent in 2D produces a velocity field whose effective Hölder exponent is shifted by $-1/2$: a nominal $\zeta = 1/3$ becomes an actual $-1/6$, which is in the non-Hölder, cutoff-dominated regime. The correct 2D exponent is $2\zeta + d = 8/3$ for $d = 2$, $\zeta = 1/3$. We have verified explicitly that the synthetic flow with this corrected exponent satisfies $S_2(r) \propto r^{2/3}$ within $\sim 20\%$ across the inertial range.*

d. Computational cost. Generating $v(x, t)$ on an N_{grid}^d -grid requires one inverse FFT per time step, $O(N_{\text{grid}}^d \log N_{\text{grid}})$. For the deform-cloud scheme we evaluate v pointwise at the particle cloud, which costs $O(N \cdot |\Lambda|)$ per step — linear in the number of particles and the number of retained Fourier modes.

A. Time Correlations and Anchoring the Cloud

a. Delta-correlated case: the Kraichnan limit. Drawing $a_k(t)$ as a fresh complex Gaussian random variable at each discrete time step Δt , with variance scaled as $\propto \Delta t$, reproduces in the $\Delta t \rightarrow 0$ limit a velocity field $v(x, t)$ with two-time covariance

$$\mathbb{E}[v_\alpha(x, t) v_\beta(y, s)] = D_{\alpha\beta}(x - y) \delta(t - s), \quad (19)$$

where $D_{\alpha\beta}(r)$ is isotropic, incompressible, and has the prescribed Hölder structure $D_{\alpha\beta}(r) \sim r^{2\zeta}$. This is the Kraichnan model of [17]. The spectral construction is therefore a direct (and trivially isotropic) realisation of the Kraichnan model.

b. Finite time correlation. For a flow with finite Lagrangian memory, give each Fourier amplitude $a_k(t)$ an Ornstein–Uhlenbeck dynamics with wavenumber-dependent correlation

time:

$$da_k(t) = -\tau(|k|)^{-1} a_k(t) dt + \sqrt{2/\tau(|k|)} d\xi_k(t), \quad (20)$$

with $d\xi_k$ a fresh complex Gaussian noise at each instant, and $\tau(|k|)$ the per-mode correlation time. The natural physical choice is the local eddy-turnover at the corresponding scale,

$$\tau(|k|) \sim |k|^{-(1-\zeta)} \sim \ell^{1-\zeta}, \quad \ell = 1/|k|, \quad (21)$$

which gives the Kolmogorov scaling $\tau \sim \ell^{2/3}$ at $\zeta = 1/3$ and scale-independent memory in the Batchelor limit $\zeta = 1$.

c. Anchoring the cloud. The synthetic velocity field is generated in Fourier space, with prescribed Ornstein–Uhlenbeck dynamics of the Fourier amplitudes. Therefore the large-scale sweeping ambiguity of Eulerian real-space two-time measurements is not the central issue here. The deform-cloud diagnostic probes relative deformation of a cloud, and the absolute translation of the cloud centroid is a nuisance variable.

We remove this nuisance by retaining only the sine sector of the Fourier expansion, equivalently $\hat{v}_k(t) = i b_k(t)$, $b_{-k} = -b_k$, $b_k \in \mathbb{R}^d$. Then $v(x, t) = \sum_{k>0} 2P(k)b_k(t) \sin(2\pi k \cdot x/L)$, and consequently $v(0, t) \equiv 0$, $\nabla v(0, t) \neq 0$. A cloud initialized at the origin therefore remains anchored there, while still experiencing a nontrivial stochastic velocity gradient. The sine-sector restriction should be understood as a convenient quasi-Lagrangian centering device, not as an essential physical ingredient of the deform-cloud mechanism. With a full sine–cosine field one would instead follow the moving cloud centroid and work in relative coordinates.

B. Historical context

a. Kraichnan’s original construction. Kraichnan (1968, [17]) introduced the model (19) as a tractable Eulerian random velocity field for studying passive-scalar advection in incompressible turbulence. The two-time δ -correlation is the technical simplification that makes the multi-point passive-scalar moment equations linear, with the spatial Hölder structure inherited from a prescribed $D_{\alpha\beta}(r)$. Kraichnan’s 1968 paper, and his follow-up *J. Fluid Mech.* paper of 1974 on quasi-uniform straining, established the model as the principal analytic testbed for the question of anomalous scaling — an open question for the next quarter century.

b. The 1995 resolution of anomalous scaling. Three independent groups [9–11] reached the shared conclusion: anomalous scaling is governed by zero modes — equivalently, by statistically conserved quantities along Lagrangian trajectories. The Lagrangian description of multi-particle dynamics in the Kraichnan flow is the technical machinery that made the analysis tractable; this is the direct intellectual ancestor of the tetrad model of [2] and of the ellipsoid construction of Part I.

c. Stepanov’s anisotropic shear construction. In unpublished notes [1], M. Stepanov developed a constructive realisation of an essentially Kraichnan-class flow as a composition of one-dimensional shears: at each atomic time step, motion along one coordinate axis by an amount depending on the other coordinates, alternating between axes. The construction is manifestly incompressible at each atomic step but is anisotropic at every instant. In the isotropisation $\Delta t \rightarrow 0$ limit with randomised shear directions, the Stepanov construction recovers the same Kraichnan-class flow as the spectral construction (15)–(16); this is a Trotter-like decomposition of the isotropic incompressible Kraichnan generator into single-direction shear generators.

d. The Kraichnan analogy at the level of methodology. The relevance of the Kraichnan passive-scalar story for the present work is methodological. Kraichnan’s model was, deliberately, less physical than full Navier–Stokes: the velocity was Gaussian, white-in-time, with prescribed roughness; there was no cascade dynamics, no coherent structures, no temporal coherence beyond delta-correlation. The model was important not because it captured all of turbulence but because it isolated — in a tractable setting — a specific mechanism (statistically conserved zero modes) responsible for anomalous scaling, and that mechanism turned out to carry over to richer flows where the velocity is non-Gaussian and time-correlated.

The deform-cloud scheme on a Kraichnan–Stepanov flow at fixed ζ has the same character. The flow is simpler than Navier–Stokes (Gaussian, prescribed Hölder, OU per-mode correlation; no cascade dynamics, no intermittency, no coherent vortices), and the scheme on this flow yields a clean baseline phenomenology with specific mechanisms (alignment-driven shape saturation, scale-dependent perceived-gradient extraction) that should carry over qualitatively to richer flows. Real-flow applications — HIT in 3D, convection, aerodynamic boundary layers — will modify quantitative values; the methodology paper’s job is to establish the baseline against which those modifications are deltas.

IV. EMPIRICAL PHENOMENOLOGY AT $\zeta = 1/3$: EULERIAN-SIMPLE, LAGRANGIAN-NONTRIVIAL

The Kraichnan–Stepanov flow is simple on the Eulerian side: Gaussian Fourier modes, imposed incompressibility, prescribed Hölder exponent, and scale-dependent OU memory. The Lagrangian cloud produced by this flow is not simple. Its ellipsoid shape is generated by multiplicative stretching, rotation, finite-scale averaging, and the history of alignment between the coarse-grained gradient and the ellipsoid geometry. The empirical section therefore reports the phenomenology of the measured train (M, g) before any reduced model is fitted. The empirical shape and gradient statistics are collected in Figs. 2 and 3, while the source–sink mechanism is isolated in Fig. 4.

All quantities below are computed from volume-filled clouds and the outer Löwner–John ellipsoid. The reported numbers are representative of the baseline run at $\zeta = 1/3$, $K_{\max} = 60$, $N = 300$, $T = 15$, and twelve independent flow realizations. They should be understood as the synthetic-flow baseline rather than universal constants.

A. Shape statistics

Empirical finding 1 (Aspect ratio is $O(1)$, but not self-averaged). *The log-aspect-ratio*

$$\sigma(t) = \frac{1}{2} \log \frac{\lambda_+(g(t))}{\lambda_-(g(t))} \quad (22)$$

reaches an $O(1)$ level over the inertial-range bins. In the baseline run the conditional means are approximately

$$\langle \sigma \mid r \rangle \simeq (0.93, 1.08, 1.03, 0.88, 0.95, 0.80, 0.79). \quad (23)$$

Thus the MEE cloud is neither nearly circular nor indefinitely stretching. The distribution is broad, however: the conditional standard deviation is typically 30–50% of the mean. We therefore avoid the stronger phrase “self-averaging.” The correct empirical statement is that σ has an $O(1)$ quasi-stationary level with substantial fluctuations.

The distributional test is the family of conditional laws $P(\sigma \mid r)$ and their pairwise Kolmogorov–Smirnov distances. Approximate stability of $P(\sigma \mid r)$ in the middle bins is meaningful, but the large- r and smallest- r bins retain finite-range and finite-time effects.

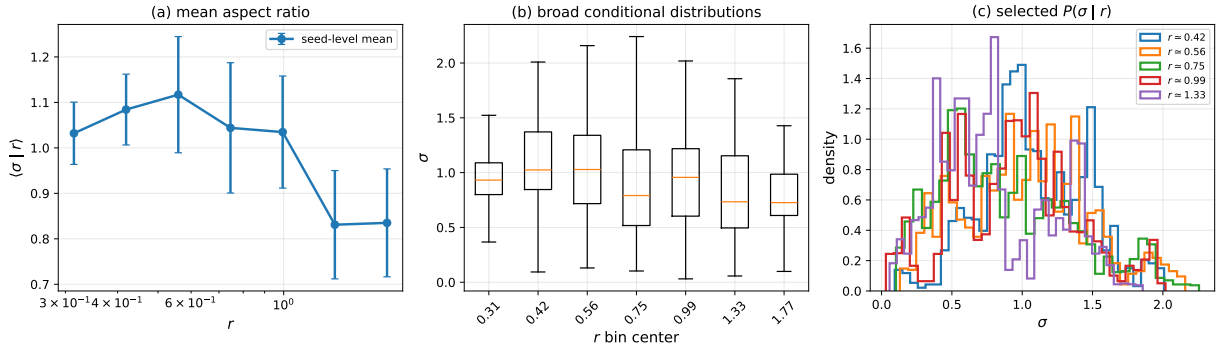


Figure 2. **Empirical MEE shape statistics.** The log-aspect-ratio σ is an $O(1)$ fluctuating state variable. Panel (a) shows $\langle \sigma | r \rangle$ with seed-level uncertainty. Panels (b,c) show that the conditional distributions are broad and retain visible scale dependence.

Both mean and distribution should therefore be shown in the paper; the mean alone is insufficient. Figure 2 reports these complementary summaries.

B. Gradient scaling and corrected strain–vorticity balance

Write

$$M = \begin{pmatrix} s_+ & s_\times + \omega \\ s_\times - \omega & -s_+ \end{pmatrix}, \quad (24)$$

so that (s_+, s_\times) are the symmetric traceless strain components and ω is the antisymmetric component. We use the reduced norm

$$|M|_{\text{red}}^2 = s_+^2 + s_\times^2 + \omega^2, \quad (25)$$

which differs from the Frobenius norm by the constant factor two.

Empirical finding 2 (Steep scale dependence of the ellipsoid-averaged gradient). *The dimensional expectation for a Hölder- ζ velocity field is*

$$\langle |M|^2 | r \rangle \sim r^{2(\zeta-1)}, \quad (26)$$

hence $r^{-4/3}$ at $\zeta = 1/3$. The cleaned MEE-averaged train gives a steeper effective slope, close to -2 in the present finite-range experiment. We report this as an empirical property of the diagnostic rather than force agreement with the dimensional estimate. Plausible contributors

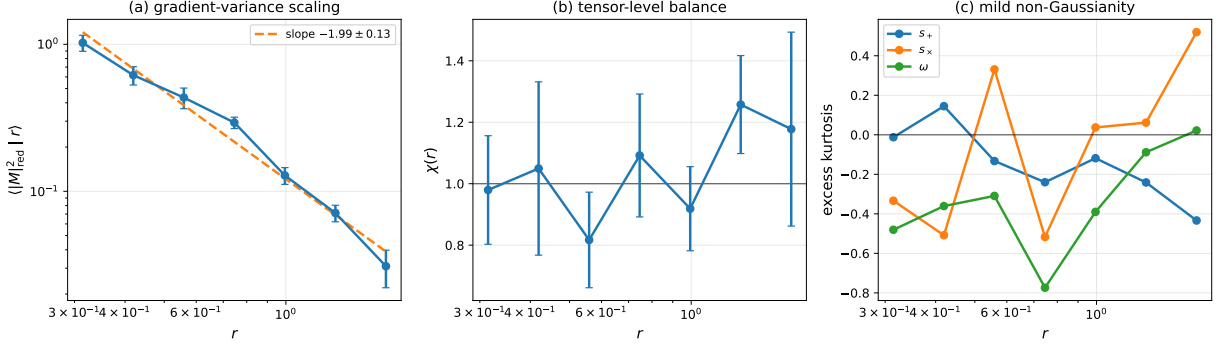


Figure 3. **Coarse-grained gradient statistics.** Panel (a) shows the scale dependence of $\langle |M|_{\text{red}}^2 | r \rangle$. Panel (b) shows the corrected tensor-level strain–vorticity ratio $\chi(r)$, with $\chi = 1$ corresponding to ordinary two-dimensional incompressible balance. Panel (c) summarizes the mild component non-Gaussianity of the rescaled gradient.

are the finite spectral cutoff, the soft Bessel filter in the ellipsoid average, finite inertial range, and the fact that the averaging region is an elongated Lagrangian ellipsoid rather than an isotropic ball.

Empirical finding 3 (Strain–vorticity balance). *The component-level relation*

$$\text{var}(\omega) : \text{var}(s_+) : \text{var}(s_\times) = 2 : 1 : 1 \quad (27)$$

is the standard kinematic normalization for a two-dimensional incompressible isotropic gradient. The tensor-level diagnostic is

$$\chi(r) = \frac{\text{Var}(\omega | r)}{\text{Var}(s_+ | r) + \text{Var}(s_\times | r)}, \quad (28)$$

whose incompressible isotropic baseline is $\chi = 1$. In the baseline run χ remains of order one – roughly balanced.

Empirical finding 4 (Mild non-Gaussianity). *The components of the rescaled gradient are approximately Gaussian but not exactly. Since the underlying spectral velocity field is Gaussian, the observed deviations should be interpreted as effects of finite-time Lagrangian conditioning, ellipsoid averaging, and shape selection rather than as intrinsic non-Gaussianity of the Eulerian synthetic field. The corresponding gradient diagnostics are shown together in Fig. 3.*

C. Intrinsic variables and the source–sink identity

The intrinsic variables introduced in (5) make the mechanism behind the aspect-ratio dynamics explicit. In the ellipsoid frame, the strain contribution to the growth of σ is

$$2S'_{11} = 2A \cos \alpha,$$

so the empirical train defines the residual

$$R_\sigma = \dot{\sigma} - 2A \cos \alpha. \quad (29)$$

Thus (6) is not an imposed closure but an empirical decomposition of the measured MEE dynamics. The source $2A \cos \alpha$ is positive when the ellipsoid axis is preferentially aligned with the principal stretching direction; the residual R_σ collects the finite-cloud and Löwner–John effects that are absent from the material ellipsoid equation.

This decomposition is the bridge to the generator-identification section. A marginal stochastic model for M can reproduce some one-time statistics of the coarse-grained gradient, but if it destroys the joint alignment encoded in α , then the source $2A \cos \alpha$ disappears and the model cannot generate the observed $O(1)$ aspect ratio. The fitted closure below therefore preserves the source term in (6) and only parameterizes the residual R_σ , ultimately by the affine form (7).

In the baseline run the conditional source and residual have opposite signs. The source $2A \cos \alpha$ is positive over most scale bins, while R_σ is negative. Their near-cancellation explains why σ remains $O(1)$ rather than growing without bound. This is the main physical conclusion of the empirical analysis: *The MEE aspect ratio is maintained by a balance between aligned strain, which stretches the ellipsoid, and an effective Löwner–John residual, which relaxes the ellipsoidal summary of the deforming cloud.* This statement is empirical and diagnostic-level. It does not assert that the same numerical balance will hold in DNS or experiments; rather, it defines the mechanism to be tested there. Fig. 4 shows this decomposition and its near-cancellation across scale bins.

D. Summary of empirical findings

- The MEE aspect ratio satisfies $\sigma = O(1)$ but remains broadly distributed.

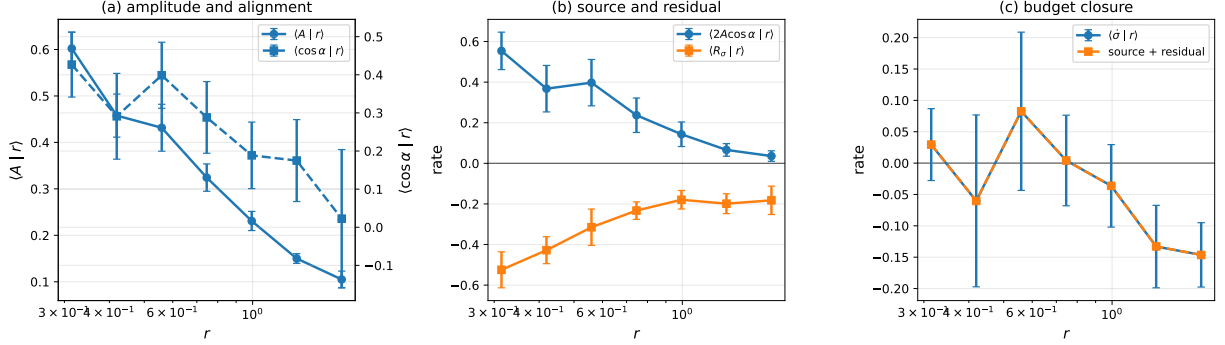


Figure 4. **Empirical source–sink mechanism.** The aspect-ratio dynamics of the MEE train is decomposed as $\dot{\sigma} = 2A \cos \alpha + R_\sigma$, where $A = |S|$ is the strain amplitude, α is the doubled angle between the principal strain direction and the ellipsoid major axis, and $R_\sigma = \dot{\sigma} - 2A \cos \alpha$ is the effective Löwner–John residual. (a) The strain amplitude $\langle A | r \rangle$ decreases with scale, while the alignment bias $\langle \cos \alpha | r \rangle$ remains positive over most of the sampled range. Thus the ellipsoid is statistically biased toward the stretching direction, producing a positive aligned-strain source. (b) The source $\langle 2A \cos \alpha | r \rangle$ is positive, whereas the empirical residual $\langle R_\sigma | r \rangle$ is negative. The two terms therefore act as competing source and sink contributions to the aspect-ratio dynamics. (c) Their sum nearly closes the measured drift $\langle \dot{\sigma} | r \rangle$, showing that the observed $O(1)$ aspect ratio is maintained by a balance between strain-induced elongation and the geometric relaxation associated with recomputing the Löwner–John ellipsoid from the deforming cloud.

- The measured M -scaling is steeper than the dimensional $-4/3$ expectation in the present finite-range experiment.
- The strain–vorticity is roughly balanced.

V. WHY THE REDUCED MODEL SHOULD BE FITTED AS A PHYSICS-INFORMED GENERATOR

We now implement the program outlined in (3)–(7). The general phenomenological SODE separates the known material-ellipsoid (passive) kinematics from the unresolved stochastic dynamics of the coarse-grained gradient and the Löwner–John projection residual. The purpose of this section is to show how the formal functions in (3) can be replaced, step by step, by a small interpretable closure identified from the empirical train.

The reduced-model problem is to construct a stochastic process whose forward simulations reproduce the empirical statistics of the train (M, g) . Thus the calibration target is the conditional short-time generator of the observed process – that is the right hand sides of Eqs. (3).

Observables such as $\langle \sigma \mid r \rangle$, $P(\sigma \mid r)$, $\chi(r)$, and $\langle |M|^2 \mid r \rangle$ are reserved for forward validation. This distinction is essential: fitting these observables directly would obscure the physical source–sink structure exposed by (6). They are validation diagnostics, not training targets.

Consider the vector of intrinsic variables

$$y(t) = (v(t), \sigma(t), A(t), \omega(t), \alpha(t)). \quad (30)$$

The generator-identification step uses short-time increments of this process, not the final conditional observables used later for validation. For a short lag Δ , define

$$\Delta_{\Delta} y_i(t) = y_i(t + \Delta) - y_i(t).$$

At the formal level, the drift and covariance of the reduced Markov generator are estimated from conditional moments,

$$\begin{aligned} b_i(y) &\simeq \Delta^{-1} \mathbb{E}[\Delta_{\Delta} y_i(t) \mid y(t) = y], \\ Q_{ij}(y) &\simeq \Delta^{-1} \text{Cov}(\Delta_{\Delta} y_i(t), \Delta_{\Delta} y_j(t) \mid y(t) = y). \end{aligned}$$

In practice we do not estimate arbitrary functions of the full five-dimensional state. Instead, physical considerations determine a low-dimensional ansatz for each component of the generator, and only the coefficients of this ansatz are fitted from the short-time increments.

For example, the final aspect-ratio closure keeps the kinematic source $2A \cos \alpha$ explicitly and regresses only the residual $R_{\sigma}(t) = \dot{\sigma}(t) - 2A(t) \cos \alpha(t)$. In each scale bin, the affine residual model $R_{\sigma} \approx a_0(r) + a_1(r)\sigma$ is obtained by the least-squares problem

$$(a_0, a_1) = \arg \min_{\beta_0, \beta_1} \sum_{n \in \mathcal{B}(r)} [R_{\sigma, n} - \beta_0 - \beta_1 \sigma_n]^2,$$

with a small ridge penalty added when needed for numerical stability. The same logic is used for the scale-dependent stochastic drivers: the conditional means and variances of the increments of A and ω are fitted in r -bins to the chosen OU-type parametrization.

Thus the calibration is a sequence of low-dimensional generator regressions, not a global black-box optimization. We do not tune parameters to match $\langle \sigma \mid r \rangle$ or other final observables. Those observables are held out as forward-validation tests: after the coefficients are fitted from short-time increments, the reduced SDE is simulated and compared with the empirical train through $\langle \sigma \mid r \rangle$, $P(\sigma \mid r)$, $\langle 2A \cos \alpha \mid r \rangle$, and the source–sink budget. This separation between generator fitting and forward validation is the reusable part of the method, and can be applied to synthetic flows, DNS, or experimental particle tracks once the Löwner–John train has been constructed.

A. Null model and why it fails

The first model to test is the most constrained one: a marginal OU process for the coarse-grained gradient combined with deterministic ellipsoid kinematics. In principal variables this gives

$$\dot{\sigma} = 2S'_{11} - \frac{1}{2}\kappa(r) \sinh(2\sigma), \quad (31)$$

with S'_{11} supplied by an M -process whose law depends only on r . This model captures parts of the one-time statistics of M , but forward simulation gives an aspect ratio close to zero rather than the empirical $O(1)$ values. The failure is qualitative.

The reason is that the marginal OU model destroys the empirical alignment between the strain and the ellipsoid axis. In the data,

$$S'_{11} = A \cos \alpha \quad (32)$$

has a positive conditional mean. In the marginal model, the orientation of the ellipsoid and the strain direction become effectively decorrelated, $\mathbb{E}[A \cos \alpha \mid r] \simeq 0$, and the model has no source capable of creating an elongated MEE cloud. This null-model failure is useful: it localizes the missing mechanism in the joint generator of the alignment variables, not in the marginal variance of M .

B. Intrinsic physics-informed closure

The null model identifies what must be repaired. The failure is not mainly that the marginal variance of M is wrong; it is that a marginal model for M destroys the joint shape–

gradient alignment encoded in α . Once $\mathbb{E}[A \cos \alpha \mid r]$ is lost, the aspect-ratio equation has no persistent positive source and the simulated ellipsoid remains nearly circular. The successful closure must therefore keep the aligned-strain source $2A \cos \alpha$ explicit and model separately the quantities that control it: the strain amplitude A , the vorticity ω , the alignment angle α , and the Löwner–John residual R_σ .

This is the reason for switching from the laboratory variables (M, g) to the intrinsic variables (30). The closure below should be read as a sequence of minimal repairs suggested by the null-model failure. First, the scale $v = \log r$ is fitted from the empirical cloud growth. Second, the marginal drivers A and ω are modeled as scale-dependent stochastic processes. Third, the alignment angle is modeled through its stationary circular bias rather than through a noisy instantaneous angular drift. Finally, after the material source $2A \cos \alpha$ is retained, the remaining Löwner–John contribution is closed by the simplest adequate residual model.

1. Scale, strain-amplitude, and vorticity drivers

The scale coordinate is fitted directly from the empirical MEE growth,

$$dv = b_v(r) dt + \sqrt{2D_v(r)} dW_v.$$

This equation is not meant to explain scale growth from first principles; it is the one-dimensional stochastic driver that reproduces the observed progression of the cloud through the inertial-range bins.

The strain amplitude and vorticity are modeled as scale-dependent OU-type drivers,

$$\begin{aligned} dA &= -\lambda_A(r)(A - \bar{A}(r)) dt + \sqrt{2D_A(r)} dW_A, \\ d\omega &= -\lambda_\omega(r)\omega dt + \sqrt{2D_\omega(r)} dW_\omega. \end{aligned}$$

This is the minimal marginal part of the closure. It reflects the empirical observation that the one-time statistics of A and ω are controlled primarily by the current ellipsoid scale r , while their direct dependence on (σ, α) is subleading at the level of the present baseline. We do not claim this OU form as a universal law; it is the simplest interpretable scale-conditioned stochastic representation consistent with the synthetic-flow train.

2. Stationary alignment closure

The null model shows that preserving the source $2A \cos \alpha$ requires a closure for the joint alignment of the strain and the ellipsoid axis. Direct regression of the angular drift $\dot{\alpha}$ is unstable in the present data: α is periodic, strongly diffusive, and sensitive to short-time wrapping errors. We therefore fit the stationary alignment bias rather than a pointwise angular drift.

At fixed (r, σ, A) , we approximate the conditional angular law by the von-Mises distribution [19, 20] – the standard circular analogue of a Gaussian distribution

$$p(\alpha | r, \sigma, A) = \frac{1}{2\pi I_0(K)} \exp(K(r, \sigma, A) \cos \alpha), \quad (33)$$

where I_0 is the modified Bessel function. The concentration K is inferred from the empirical conditional moment

$$\mathbb{E}[\cos \alpha | r, \sigma, A] = \frac{I_1(K(r, \sigma, A))}{I_0(K(r, \sigma, A))}. \quad (34)$$

The associated angular diffusion is

$$d\alpha = -D_\alpha(r)K(r, \sigma, A) \sin \alpha dt + \sqrt{2D_\alpha(r)} dW_\alpha. \quad (35)$$

This closure has the desired open-box interpretation. The ellipsoid orientation is not slaved to a deterministic angular law; instead, it samples a noisy alignment equilibrium biased toward stretching. This bias maintains a positive conditional mean of $\cos \alpha$ and hence repairs the missing source $\langle 2A \cos \alpha | r \rangle$ that was lost in the marginal OU null model.

We also tested a vorticity-driven rotation correction,

$$d\alpha = c_\omega(r)\omega dt - D_\alpha(r)K \sin \alpha dt + \sqrt{2D_\alpha(r)} dW_\alpha. \quad (36)$$

In the present baseline the fitted coefficient is noisy and degrades forward validation. We therefore keep the stationary von-Mises alignment model as the main closure and leave additional rotational corrections to future datasets where they are empirically supported.

3. Aspect-ratio residual

Once the alignment source is modeled explicitly, the remaining term in the aspect-ratio dynamics is the Löwner–John residual,

$$R_\sigma = \dot{\sigma} - 2A \cos \alpha.$$

This residual is not a small numerical correction. It is the effective geometric response of the MEE projection: the enclosing ellipsoid is recomputed from a finite, deforming cloud and is therefore not a material ellipsoid.

A natural first ansatz is the material-ellipsoid relaxation form

$$R_\sigma = -\frac{1}{2}\kappa(r)\sinh(2\sigma).$$

This form is useful as a reference, but it is too restrictive for the empirical MEE residual. In the baseline run, the simplest adequate closure is the scale-dependent affine form (7). Thus the final interpretable shape equation is

$$d\sigma = [2A \cos \alpha + a_0(r) + a_1(r)\sigma] dt + \sqrt{2D_\sigma(r)} dW_\sigma. \quad (37)$$

Eq. (37) is the open-box explanation of the saturated aspect ratio. The first term is the material aligned-strain source, the affine term is the effective Löwner–John projection response, and the diffusion represents unresolved short-time fluctuations. The model therefore tests whether the empirical source–sink balance survives forward simulation.

The closure just described is deliberately not the most flexible possible SDE. It is the smallest model in the tested hierarchy that preserves the alignment source, supplies an empirically adequate Löwner–John residual, and passes forward validation on the main shape statistics.

C. Model comparison and interpretation

The models tested above should be read as a failure-and-repair sequence, not as an exhaustive search for the best surrogate. The marginal-OU null model is included because it identifies the missing mechanism: it can reproduce some marginal statistics of M , but it destroys the alignment source $\langle A \cos \alpha \mid r \rangle$. The subsequent closures repair this failure in two steps. First, the stationary von–Mises closure restores most of the aligned-strain source. Second, the residual term in the σ equation is simplified to the smallest form that is adequate for the MEE projection residual.

For clarity we name the two von–Mises closures compared in Fig. 5. The model denoted VM0 uses the stationary von–Mises alignment closure for α , but keeps the more restrictive

nonlinear residual $R_\sigma = -\frac{1}{2}\kappa(r)\sinh(2\sigma)$. The model denoted VM1 is the final closure used in the paper: $R_\sigma = a_0(r) + a_1(r)\sigma$, together with the same von–Mises alignment model. Thus VM0 and VM1 differ only in the representation of the Löwner–John residual; the comparison tests whether the original material-ellipsoid damping form is flexible enough for the empirical MEE train.

Fig. 5 summarizes the validation. Panel (a) compares the empirical conditional mean $\langle\sigma | r\rangle$ with the marginal-OU null model, VM0, and VM1. The null model remains too close to a circular ellipsoid because it lacks the alignment source. VM0 improves the result by restoring alignment, but still underestimates the aspect ratio in several bins. VM1 gives the best compromise: it is not exact, but it reproduces the observed $O(1)$ aspect ratio over the inertial-range bins.

Panel (b) tests the most important mechanistic quantity, the aligned-strain source. It plots the model-to-empirical ratio

$$\frac{\langle 2A \cos \alpha | r \rangle_{\text{model}}}{\langle 2A \cos \alpha | r \rangle_{\text{emp}}}.$$

A value near one means that the closure preserves the source responsible for anisotropy production. This diagnostic is more informative than $\langle\sigma | r\rangle$ alone, because a model could fit the mean aspect ratio for the wrong dynamical reason.

Panel (c) compares the residual contribution R_σ . This is where the difference between VM0 and VM1 is most visible. The nonlinear $\sinh(2\sigma)$ residual is too restrictive for the MEE projection correction, whereas the affine residual gives a more faithful empirical sink. Panel (d) compresses the same conclusion into an root mean square error (RMSE) comparison across the tested hierarchy. The decrease from the null model to VM0 measures the benefit of restoring alignment; the further decrease from VM0 to VM1 measures the benefit of replacing the restrictive residual by the affine Löwner–John closure.

Notice that the agreement between the empirical train and VM1 is reasonable but imperfect and should not be overstated.

The important point is not point-wise accuracy in every bin, but preservation of the mechanism: the final open-box closure maintains the positive aligned-strain source and supplies a negative Löwner–John residual in forward simulation. We do not tune directly to the validation curves in Fig. 5; they are forward-simulation tests of a generator fitted from short-time increments.

a. Relation to more flexible data-driven closures. The present closure is intentionally low-dimensional and interpretable. This choice is consistent with the physics-informed turbulence modeling perspective reviewed in [21]: neural or diffusion-based components are most useful when they are introduced as structured residual models rather than as replacements for known physics. In the present setting this means keeping the source–sink structure – $\dot{\sigma} = 2A \cos \alpha + R_\sigma$ – and, if needed in richer flows, learning residual corrections to $K(r, \sigma, A)$, to R_σ , or to the finite-step transition law $p(y_{t+\Delta} | y_t)$. For the synthetic baseline these extensions are unnecessary; the simple open-box closure already captures the dominant anisotropy mechanism.

VI. STATUS AND OUTLOOK

This paper develops a Lagrangian diagnostic and a reduced-modeling pipeline for deforming particle clouds. The diagnostic layer maps a volume-filled tracer cloud to the outer Löwner–John ellipsoid and to the ellipsoid-averaged velocity gradient, producing the structured train $(M(t), g(t))$. The empirical layer shows that this train contains information not visible in scalar pair statistics alone: the MEE aspect ratio reaches an $O(1)$ fluctuating regime, the ellipsoid-averaged gradient has a strong scale dependence, the corrected tensor-level strain–vorticity balance remains ordinary in the synthetic baseline, and the aspect-ratio dynamics admits the source–sink decomposition $\dot{\sigma} = 2A \cos \alpha + R_\sigma$. The modeling layer then treats the train as data for physics-informed generator identification. The marginal-gradient null model fails because it destroys the joint alignment between the strain and the ellipsoid geometry. The successful open-box closure preserves the aligned-strain source and represents the remaining Löwner–John projection effect by an effective residual.

The main result is therefore methodological rather than a universal turbulence closure. On the controlled Kraichnan–Stepanov synthetic flow, the procedure turns a Lagrangian particle-cloud diagnostic into a finite-dimensional stochastic model whose terms have physical meaning. In particular, the apparently robust saturation of ellipsoid anisotropy is not merely fitted: it is resolved into a balance between persistent strain alignment, which creates anisotropy, and an effective Löwner–John residual, which limits it. This source–sink interpretation is the main explanatory payoff of the reduced model.

Several extensions are natural. First, the inner Löwner–John ellipsoid should be developed as the complementary diagnostic to the outer ellipsoid used here. The MEE follows the cloud’s outer extent, while the inner ellipsoid should be more sensitive to thinning, folding, and the loss of coherent interior volume. Comparing the two trains may separate stretching of the cloud envelope from erosion of its coherent core.

Second, the construction should be extended to three dimensions. In 3D the ellipsoid state has three principal axes, two independent shape variables, and a richer alignment geometry with the strain eigenframe and vorticity direction. This setting is closer to the original Lagrangian tetrad motivation and should allow direct comparison with homogeneous isotropic turbulence, turbulent convection, and wall-bounded or obstacle-generated flows.

Third, the generator-identification step can be made more flexible without abandoning the open-box philosophy. The present closure uses scale-dependent OU-type drivers, a stationary von–Mises alignment bias, and an affine residual. These choices were sufficient for the synthetic baseline, but richer flows may require state-dependent residuals, non-Gaussian noise, memory terms, or neural SDE components. Such extensions should be used as residual models, not as replacements for the interpretable source–sink structure.

Finally, the diagnostic should be applied to DNS and experimental particle tracks. The value of the synthetic baseline is that it provides a clean reference: future applications can ask which parts of the source–sink budget survive, which coefficients change, and which new physical mechanisms enter. In this sense the present work is a first calibration of a portable Lagrangian measurement-and-modeling framework for stochastic hydrodynamics.

ACKNOWLEDGMENTS

The author gratefully acknowledges financial support from the University of Arizona start-up program and prior support (in 2019-2024) from Los Alamos National Laboratory (LANL). The ideas developed in this paper grew out of a long-running collaboration between the University of Arizona and LANL on Machine Learning for Turbulence (MELT), with a particular focus on Lagrangian turbulence. The author is grateful to M. Stepanov, D. Livescu, C. Fryer, Y. Tian, M. Woodward, and C. Hyett for many discussions on Lagrangian transport, particle-based reduced models, and physics-informed closures.

The final development of this work took place largely in May 2026, in the aftermath of the tragic death of Misha Stepanov and in his memory, while the author was visiting Oak Ridge National Laboratory. The author gratefully acknowledges the support of ORNL through its mini-sabbatical program, and especially the hospitality and encouragement of J. Restrepo and R. Archibald.

Large language models, including Claude (Anthropic) and ChatGPT (OpenAI), were used for text editing, code refactoring, and organizational assistance. All mathematical derivations, scientific claims, numerical results, and code were independently checked and validated by the author.

CODE REPRODUCIBILITY

All computations reported in this work were performed on a standard laptop. The code, data products, provenance notebooks, and scripts used to generate the figures are available at <https://github.com/mchertkov/LagrangianEllipsoid>. The repository includes a lightweight path for reproducing the paper figures from saved data products, as well as provenance notebooks documenting the generation of the empirical train and the subsequent reduced-model calibration.

-
- [1] M. Stepanov, Synthetic-flow Lagrangian simulations with inscribed-ellipsoid (2024).
 - [2] M. Chertkov, A. Pumir, and B. I. Shraiman, *Physics of Fluids* **11**, 2394 (1999), `eprint: https://pubs.aip.org/aip/pof/article-pdf/11/8/2394/19058180/2394.1_online.pdf`.
 - [3] Y. Tian, D. Livescu, and M. Chertkov, *Physical Review Fluids* **6**, 094607 (2021).
 - [4] Y. Tian, M. Woodward, M. Stepanov, C. Fryer, C. Hyett, D. Livescu, and M. Chertkov, *Proceedings of the National Academy of Sciences* **120**, e2213638120 (2023).
 - [5] M. Woodward, Y. Tian, C. Hyett, C. Fryer, M. Stepanov, D. Livescu, and M. Chertkov, *Physical Review Fluids* **8**, 054602 (2023).
 - [6] C. Hyett, Y. Tian, M. Woodward, M. Stepanov, C. Fryer, D. Livescu, and M. Chertkov, *Lagrangian Attention Tensor Networks for Velocity Gradient Statistical Modeling* (2025), `arXiv:2502.07078 [physics]`.

- [7] G. K. Batchelor, *Journal of Fluid Mechanics* **5**, 113 (1959).
- [8] L. G. Khachiyan, *Mathematics of Operations Research* **21**, 307 (1996).
- [9] M. Chertkov, G. Falkovich, I. Kolokolov, and V. Lebedev, *Physical Review E* **52**, 4924 (1995).
- [10] K. Gawedzki and A. Kupiainen, *Physical Review Letters* **75**, 3834 (1995).
- [11] B. I. Shraiman and E. D. Siggia, *Comptes Rendus de l'Académie des Sciences, Série II* **321**, 279 (1995).
- [12] E. Aurell, G. Boffetta, A. Crisanti, G. Paladin, and A. Vulpiani, *Journal of Physics A: Mathematical and General* **30**, 1 (1997).
- [13] A. Pumir, B. I. Shraiman, and M. Chertkov, *Physical Review Letters* **85**, 5324 (2000).
- [14] L. Biferale, G. Boffetta, A. Celani, B. J. Devenish, A. Lanotte, and F. Toschi, *Physics of Fluids* **17**, 111701 (2005).
- [15] V. I. Oseledets, *Trans. Moscow Math. Soc.* **19**, 197 (1968).
- [16] L. Arnold, *Random Dynamical Systems*, Springer Monographs in Mathematics (Springer Berlin Heidelberg, Berlin, Heidelberg, 1998).
- [17] R. H. Kraichnan, *Physics of Fluids* **11**, 945 (1968).
- [18] R. H. Kraichnan, *The Physics of Fluids* **10**, 1417 (1967).
- [19] K. V. Mardia and P. E. Jupp, *Directional Statistics* (Wiley, Chichester, 2000).
- [20] N. I. Fisher, *Statistical Analysis of Circular Data* (Cambridge University Press, Cambridge, 1993).
- [21] M. Chertkov, *Journal of Physics A: Mathematical and Theoretical* **57**, 333001 (2024).

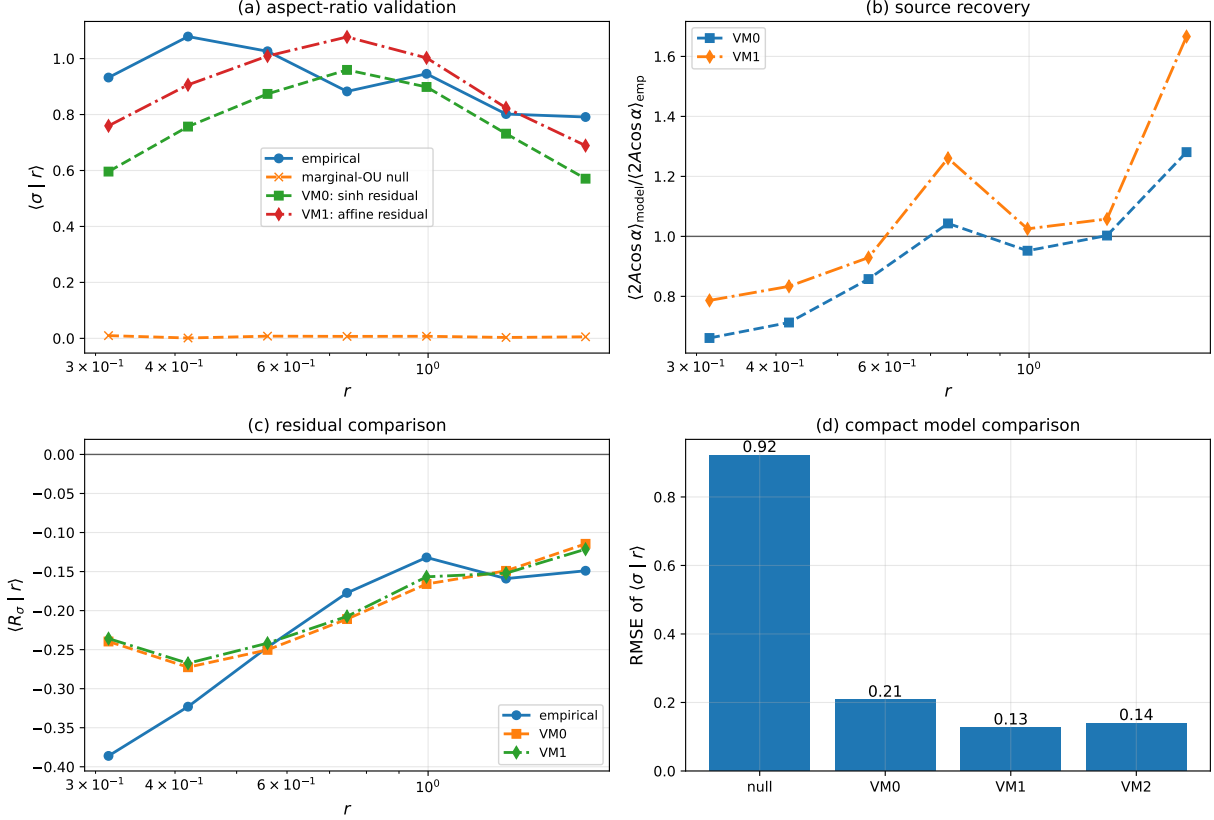


Figure 5. **Physics-informed closure validation.** (a) Conditional mean aspect ratio $\langle \sigma | r \rangle$ for the empirical train and three reduced models. The marginal-OU null model fits only marginal gradient statistics and fails because it destroys the alignment source. VM0 restores stationary von-Mises alignment for α but keeps the restrictive material-ellipsoid residual $R_\sigma = -\frac{1}{2}\kappa(r) \sinh(2\sigma)$. VM1 is the final closure used in the paper: it uses the same von-Mises alignment model and replaces the residual by the affine Löwner-John form $R_\sigma = a_0(r) + a_1(r)\sigma$. (b) Recovery of the aligned-strain source, shown as the ratio $\langle 2A \cos \alpha | r \rangle_{\text{model}} / \langle 2A \cos \alpha | r \rangle_{\text{emp}}$. Values near one indicate that the closure preserves the mechanism producing anisotropy. (c) Residual comparison, showing $\langle R_\sigma | r \rangle$ for the empirical train and the reduced models. The affine residual in VM1 gives a more faithful effective sink than the restrictive VM0 form. (d) Compact RMSE comparison of the tested hierarchy. VM2 is a richer source-aware residual diagnostic, $R_\sigma = a_0(r) + a_1(r)\sigma + a_2(r)A + a_3(r)A \cos \alpha$. It is included to show that adding explicit source dependence does not improve the validation enough to justify the extra parameters. The selected closure is therefore VM1, the simplest model that restores the alignment source and gives an adequate Löwner-John residual.